


# Pseudocapacitive Heteroatom-Doped Carbon Cathode for Aluminum-Ion Batteries with Ultrahigh Reversible Stability

Jiahui Li, Jehad K. El-Demellawi, Guan Sheng, Jonas Björk, Fanshuai Zeng, Jie Zhou, Xiaxia Liao, Junwei Wu, Johanna Rosen\*, Xingjun Liu\*, Husam N. Alshareef, and Shaobo Tu\* 

**Aluminum (Al)-ion batteries have emerged as a potential alternative to conventional ion batteries that rely on less abundant and costly materials like lithium. Nonetheless, given the nascent stage of advancement in Al-ion batteries (AIBs), attaining electrode materials that can leverage both intercalation capacity and structural stability remains challenging. Herein, we demonstrate a C<sub>3</sub>N<sub>4</sub>-derived layered N,S heteroatom-doped carbon, obtained at different pyrolysis temperatures, as a cathode material for AIBs, encompassing the diffusion-controlled intercalation and surface-induced capacity with ultrahigh reversibility. The developed layered N,S-doped carbon (N,S-C) cathode, synthesized at 900 °C, delivers a specific capacity of 330 mAh g<sup>-1</sup> with a relatively high coulombic efficiency of ~85% after 500 cycles under a current density of 0.5 A g<sup>-1</sup>. Owing to its reinforced adsorption capability and enlarged interlayer spacing by doping N and S heteroatoms, the N,S-C900 cathode demonstrates outstanding energy storage capacity with excellent rate performance (61 mAh g<sup>-1</sup> at 20 A g<sup>-1</sup>) and ultrahigh reversibility (90 mAh g<sup>-1</sup> at 5 A g<sup>-1</sup> after 10 000 cycles).**

(i.e., 2980 mAh g<sup>-1</sup>), low cost, and increased environmental security,<sup>[1–6]</sup> the shortage of efficient cathode materials that can sufficiently intercalate/de-intercalate Al<sup>3+</sup> or tetrachloroaluminate ([AlCl<sub>4</sub>]<sup>-</sup>) has substantially hindered the development of this technology.<sup>[7–9]</sup> Over the past decade, several categories of cathode materials, including transition metal oxides/chalcogenides, carbon-based materials, and MXenes, among others, have been developed to break the capacity ceiling of AIBs.<sup>[10–13]</sup> For instance, when used as cathode materials for AIBs, transition metal oxides usually demonstrate a high discharge capacity in the first few dozen cycles due to the sufficient intercalation of Al<sup>3+</sup> in their crystal structure. Lynden's group<sup>[10]</sup> utilized vanadium pentoxide (V<sub>2</sub>O<sub>5</sub>) as a cathode material for AIBs, achieving a capacity of 305 mAh g<sup>-1</sup> at a current density of 125 mA g<sup>-1</sup> in the first cycle, followed by a fast decay after 20 cycles. Damien's group<sup>[11]</sup> achieved reversible Al<sup>3+</sup> insertion in anatase

## 1. Introduction

Although aluminum-ion batteries (AIBs) are promising for mobile and large-scale energy storage due to their high theoretical specific capacity


J. Li, Dr. G. Sheng, F. Zeng, Prof. X. Liao, Prof. S. Tu  
School of Physics and Materials Science, Nanchang University, 999 Xuefu Road, Honggutan District, Nanchang 330031, China  
E-mail: [shaobo.tu@ncu.edu.cn](mailto:shaobo.tu@ncu.edu.cn)

J. Li, Prof. J. Wu, Prof. X. Liu  
School of Materials Science and Engineering, and Institute of Materials Genome and Big Data, Harbin Institute of Technology, Shenzhen 518055, China  
E-mail: [xjliu@hit.edu.cn](mailto:xjliu@hit.edu.cn)

Dr. J. K. El-Demellawi  
KAUST Upstream Research Center (KURC), EXPEC-ARC, Saudi Aramco, Thuwal 23955, Saudi Arabia

Dr. J. Björk, Dr. J. Zhou, Prof. J. Rosen  
Materials Design Division, Department of Physics, Chemistry and Biology (IFM), Linköping University, SE-581 83, Linköping, Sweden  
E-mail: [johanna.rosen@liu.se](mailto:johanna.rosen@liu.se)

Prof. H. N. Alshareef, Prof. S. Tu  
Physical Science and Engineering (PSE) Division, King Abdullah University of Science and Technology, Thuwal 23955, Saudi Arabia

 The ORCID identification number(s) for the author(s) of this article can be found under <https://doi.org/10.1002/eem2.12733>.

DOI: 10.1002/eem2.12733

TiO<sub>2</sub> for AIBs by introducing a large number of titanium vacancies as intercalation sites, leading to a discharge capacity of 120 mAh g<sup>-1</sup> at a low current density (20 mA g<sup>-1</sup>). Furthermore, due to their weaker Al–S and Al–Se bonds than Al–O bonds, transition metal chalcogenides have presented optimized reversibility for Al<sup>3+</sup> in AIBs. Lianzhou's group<sup>[12]</sup> fabricated Co<sub>9</sub>S<sub>8</sub>@CNT–CNF nanocomposites as cathode material for AIBs, offering a high specific capacity (315 mAh g<sup>-1</sup> in the first cycle) and a relatively longer cyclic performance (over 200 cycles). Nonetheless, cathodes made of either transition metal oxides or chalcogenides often suffer from a rapid decline in electrochemical performance due to the structural collapse induced by the high volumetric change during the (dis)-charging process.

In contrast, carbon-based cathode materials for Al ion batteries have raised great attention due to their high structural stability. In 2015, Dai's group<sup>[14]</sup> fabricated a rechargeable AIB with high rate capacity using a three-dimensional (3D) graphitic-foam cathode with an Al–metal anode. Although the manufactured battery could withstand more than 7500 cycles at a current density of 4 A g<sup>-1</sup>, the 3D graphitic foam failed to provide sufficient interlayer spacing for intercalating Al<sup>3+</sup>/[AlCl<sub>4</sub>]<sup>-</sup>, leading to a gravimetric capacity (65 mAh g<sup>-1</sup>), which is unfavorable for commercial cathodes of AIBs. Attempting to improve the specific capacity of carbon-based cathode materials for AIBs, Yin's group<sup>[15]</sup> designed a metal–organic framework (MOF)-derived

N,P-doped C@N-C@N,P-C hetero-structure, forming a built-in interfacial electric field as a result of the gradient N,P-doping concentration. The fabricated battery exhibited a  $\sim 90 \text{ mAh g}^{-1}$  capacity at a high current density of  $5 \text{ A g}^{-1}$  after 2500 cycles. In 2017, another carbon-based material, i.e.,  $\text{V}_2\text{CT}_x$  MXene, was utilized as a cathode for AIBs,<sup>[16]</sup> delivering a specific capacity of  $90 \text{ mAh g}^{-1}$  at a (dis)-charging current density of  $100 \text{ mA g}^{-1}$  after 100 cycles. Later, in 2022, we developed a calcined  $\text{Nb}_2\text{CT}_x$  MXene cathode for AIBs,<sup>[17]</sup> maintaining a capacity of  $108 \text{ mAh g}^{-1}$  at a current density of  $200 \text{ mA g}^{-1}$  after 500 cycles, thanks to the tunable interlayer spacing of the MXene nanosheets that allowed for the reversible (de)-intercalation of  $[\text{AlCl}_4]^-$ .

Building upon the implications of the previous developments in carbon-based cathode materials for AIBs, a trade-off between the intercalation capacity and structural stability of the cathode materials has to be achieved to allow for high-performing AIBs with adequate storage capacity and reversibility performance. For that, introducing an extra energy storage mechanism can be one implementable route to overcome the inevitable limitations of intercalation, e.g., surface adsorption, allowing for AIBs with additional storage capacity. In this regard, heteroatom doping has been deemed a feasible methodology for adjusting surface physicochemical properties and interlayer spacing of cathode materials.<sup>[18–22]</sup> Herein, we demonstrate a rechargeable AIB, embedded with nitrogen and sulfur co-doped carbon cathode against an Al–metal anode and operating with an ionic liquid–based electrolyte, i.e., 1-ethyl-3-methylimidazolium chloride [EMIm]Cl/ $\text{AlCl}_3$ . The introduction of the N and S heteroatoms has offered more active sites for surface adsorption, allowing for high storage capacity. In principle, the synergy between the pyridinic, pyrrolic, and graphitic N configurations gives rise to carbon frameworks with tailorable interlayer spacing (*d*-spacing) and versatile electronic configurations,<sup>[23,24]</sup> further enhancing the intercalation and adsorption of  $[\text{AlCl}_4]^-$  moieties. In this work, the layered N,S-doped carbon cathode exhibits a sufficiently high specific capacity of  $\sim 330 \text{ mAh g}^{-1}$  at a current density of  $0.5 \text{ A g}^{-1}$  after 500 cycles in AIBs. Furthermore, the developed batteries have unexpectedly exhibited high reversibility over 10 000 cycles with a specific capacity of  $\sim 90 \text{ mAh g}^{-1}$  and capacity retention of 97% at a practically high current density of  $5 \text{ A g}^{-1}$ . To gain more insight into the energy storage mechanism, Raman spectroscopy, X-ray photoemission spectroscopy (XPS), photoemission spectroscopy in air (PESA), high-resolution transmission electron microscopy (HRTEM), X-ray diffraction (XRD), as well as complementary density functional theory (DFT) calculations, were utilized to investigate the evolution in the microstructure and surface chemistry of the cathode materials.

## 2. Results and Discussion

Instead of using metallic catalyst-induced growth followed by acid treatment,<sup>[22]</sup> we developed a catalyst-free synthesis route for N,S-doped carbon (N,S-C), utilizing melamine as a precursor. As schematically presented in Figure 1a, a few-layered graphitic carbon nitride ( $\text{g-C}_3\text{N}_4$ ) precursor was fabricated by calcining the melamine in air at  $500^\circ\text{C}$  for 3 h. Afterwards, glucose and dithiooxamide (DTO) were proportionally added to the resultant  $\text{g-C}_3\text{N}_4$ , which was then subjected to different pyrolysis reactions ( $T = 800, 900, \text{ and } 1000^\circ\text{C}$ ) to obtain the N,S-C800, N,S-C900 and N,S-C1000 cathodes. Fourier-transform infrared (FTIR) spectroscopy confirmed the N and S doping in the layered carbon layers. The corresponding FTIR spectra of the N,S-C cathodes, illustrated in Figure S1, Supporting Information show the characteristic

vibrational bands related to C–S ( $615.7 \text{ cm}^{-1}$ ), C=S ( $1099.34 \text{ cm}^{-1}$ ), C–N ( $1629.17 \text{ cm}^{-1}$ ), and N–H ( $3417.24 \text{ cm}^{-1}$ ), respectively,<sup>[25]</sup> indicating the successful doping of N and S in the carbon frameworks.

The crystal structures of the as-synthesized  $\text{g-C}_3\text{N}_4$  and the attained N,S-C were investigated using XRD. As shown in Figure 1b, the corresponding XRD pattern of the intermediate  $\text{g-C}_3\text{N}_4$  exhibits a sharp typical (002) characteristic peak at  $2\theta = 27.4^\circ$ ,<sup>[26]</sup> while the (002) peak of N,S-C products is located at  $2\theta = 21.87^\circ$ , indicating an interlayer spacing of  $4.07 \text{ \AA}$ . Such an enlarged *d*-spacing was further verified using HRTEM, as displayed in Figure 1e. Compared to the interlayer distance of graphite ( $3.36 \text{ \AA}$ ),<sup>[27]</sup> the increase in the *d*-spacing between adjacent planes along the (001) stacking direction of carbon sheets allows for accommodating more intercalated  $[\text{AlCl}_4]^-$  ions and thus achieving higher capacity.<sup>[28,29]</sup> The corresponding Raman spectra of the N,S-C synthesized at 800, 900, and  $1000^\circ\text{C}$ , are displayed in Figure 1c, featuring the characteristic D and G bands at around  $1355$  and  $1580 \text{ cm}^{-1}$ , respectively. While the latter band is attributed to the E<sub>2g</sub> vibrational mode of the sp<sup>2</sup>-carbon atoms, the D peak, following previous reports,<sup>[30–32]</sup> can be ascribed to the activated A<sub>1g</sub> vibrational mode of the C<sub>6</sub> rings, probably induced by the defects related to the N and S doping. It is worth mentioning that the D/G intensity ratio ( $I_D/I_G$ ) of N,S-C800, 900, and 1000 is 1.063, 1.013, and 1.079, respectively, suggesting a higher degree of graphitization and a lower structural imperfection in the N,S-C900 sample compared to the other two samples. An indication of the structural imperfection in the N,S-C800 and N,S-C1000 samples is demonstrated by the corresponding HRTEM images (Figure S2, Supporting Information), confirming the lower crystallinity of the N,S-C800, in particular, which can be attributed to the lower pyrolysis temperature. Nonetheless, all the N,S-C nanosheets have maintained a clothing-like morphology, as shown in the corresponding TEM images in Figure S2, Supporting Information (N,S-C800 and N,S-C1000) and Figure 1d (N,S-C900). Further, the performed HRTEM revealed the periodic hexagonal arrangement of the carbon atoms within the heteroatom-doped carbon framework, as demonstrated in Figure 1f and Figure S3, Supporting Information for N,S-C900. The presence of the doped N and S atoms was confirmed by the obtained wide scan XPS survey spectra of all the N,S-C samples (Figure S4, Supporting Information). Meanwhile, the chemisorption interaction between the doped elements and the carbon atoms was further verified using high-resolution XPS, with the corresponding C 1s core level XPS spectra of all samples (Figure S4, Supporting Information) featuring three fitted components, attributed to the C–C ( $284.7 \text{ eV}$ ), C–S ( $285.6 \text{ eV}$ ), and C–N ( $286.7 \text{ eV}$ ) species.<sup>[33–35]</sup> The corresponding energy dispersive X-ray (EDX) elemental mapping of all samples, obtained in conjunction with TEM imaging, has revealed the homogeneous distribution of the N and S doping over the carbon-based nanosheets (Figure 1g; Figures S5 and S6, Supporting Information), with a gradual decrease in the N doping concentration as the calcination temperature rises (Table S1, Supporting Information). Nonetheless, the S doping content reached its highest value (i.e., 0.53%) for samples calcined at  $900^\circ\text{C}$ . Noteworthy, the increased S doping concentration in the N,S-C900 sample, along with the reduced amount of its O terminations (indicated by the near-absence of the C=O component in Figure S4, Supporting Information), has endowed it with a higher potential for fast de-intercalation of the ionic moieties, owing to the lower electronegativity of the S atoms.<sup>[36]</sup> The porosity and the surface area of the heteroatom-doped N,S-C nanosheets were probed using Brunauer–Emmett–Teller (BET) surface area analysis. Figure S7 and Table S2,

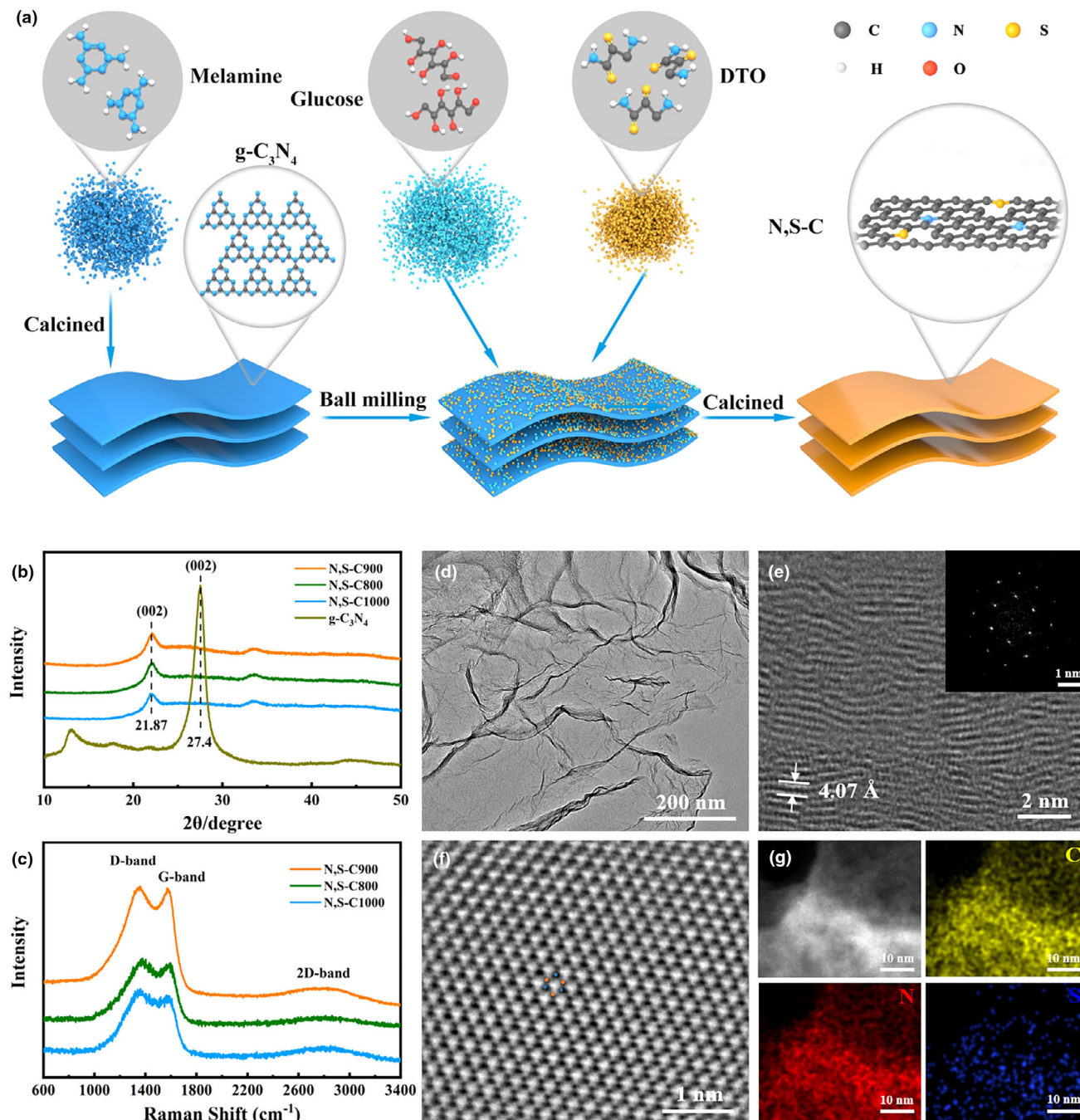
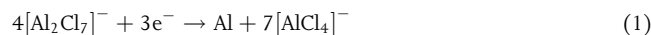


**Figure 1.** a) Schematic illustration of the synthetic routes for the fabrication of N,S-C. b) X-ray diffraction patterns of  $g\text{-C}_3\text{N}_4$  and N,S-C synthesized at 800, 900, and 1000 °C. c) Raman spectra of N,S-C800, 900, 1000. d) TEM, and e, f) HRTEM of N,S-C900. Inset: Selected area electron diffraction (SAED) pattern of N,S-C900 along the (001) axis. g) EDX of N,S-C900 and the corresponding elemental mappings: carbon, nitrogen, sulfur.

Supporting Information present the corresponding  $\text{N}_2$  adsorption-desorption analysis of the as-synthesized N,S-C nanosheets, indicating the gradual increase in the specific surface area and pore volume with the increase in the pyrolysis temperature (i.e.,  $\text{N,S-C800} < \text{N,S-C900} < \text{N,S-C1000}$ ), which may help the cathodes to infiltrate the ionic liquid electrolyte.

We assembled the Al/N,S-C Swagelok batteries using N,S-C as a cathode, aluminum foil as an anode, and [EMIm]Cl/ $\text{AlCl}_3$  ionic liquid as the electrolyte. The redox reactions of the Al/N,S-C battery during (dis)-charging can be described as:





with  $n$  denoting the molar ratio of carbon atoms in the carbon matrix to the intercalated  $[\text{AlCl}_4]^-$ . The structural evolution of all the cathode materials during the (dis)-charging process was investigated using XRD, Raman, and XPS. However, owing to its structural quality, higher crystallinity, and surface-rich S terminations compared to its counterparts (i.e., N,S-C800 and N,S-C1000), the N,S-C900 sample was selected as a model system, which was found to be the optimum N,S-C cathode as will be discussed later in this article. The ex-situ XRD patterns of the N,S-C900 cathode before testing, after fully charging, and fully discharging are presented in **Figure 2a**, showing the increase in the  $d$ -spacing of the N,S-C900 nanosheets from 4.07 Å (21.87°) to 4.3 Å (20.63°) after full charging, then contracting to 4.1 Å (21.73°) when fully discharged. Given that the size of the  $[\text{AlCl}_4]^-$  moieties ( $\sim 5.28$  Å), i.e., larger than the  $d$ -spacing of N,S-C900, the  $[\text{AlCl}_4]^-$  moieties were distorted while being intercalated in between the N,S-doped carbon interlayers.<sup>[37]</sup> After fully discharging, the recovered (002) XRD peak of the N,S-C900 cathode exhibited a broader shoulder, indicating the change of the stacking arrangements between the carbon layers as a result of the trapping of the residual  $[\text{AlCl}_4]^-$  moieties within the interlayer spacing of the N,S-C900 nanosheets.

The corresponding high-resolution XPS spectra of the N,S-C900 cathode, presented in **Figure 2d,e**, showing the decreased signal of the Al 2p and Cl 2p core level spectra after fully discharging, is indicative of the partial (de)-interaction of  $[\text{AlCl}_4]^-$  moieties after discharging,<sup>[38]</sup> which accords well with the XRD results (**Figure 2a**). **Figure 2b** depicts the incremental change in the Raman spectra of N,S-C900 during the whole (dis)-charging process, showcasing the effect of the insertion of  $[\text{AlCl}_4]^-$  within the N,S-C900 cathode. During charging from 0.01 to 2.25 V, the pristine D peak at  $\sim 1355$   $\text{cm}^{-1}$  was shifted to lower

frequencies and the pristine G peak at  $\sim 1580$   $\text{cm}^{-1}$  was shifted to higher frequencies. Both the D peak and the G peak show a simultaneous waning intensity during the charging process, leading to a decreasing  $I_D/I_G$  ratio from 1.013 to 0.953. The eventual decrease in  $I_D/I_G$  can be ascribed to a change in the electronic band structure due to the increase in the  $[\text{AlCl}_4]^-$  content, which has led to the occupation of empty states, restraining the creation of electron-hole pairs for defect-induced double-resonance. When discharging from 2.25 to 0.01 V, both D and G peaks are restored to their original position, and are accompanied by the peak enhancement due to the de-intercalation of  $[\text{AlCl}_4]^-$  from the N,S-C900 cathode.<sup>[39]</sup> Furthermore, to gain insight into the configurational evolution of the doped S and N within the carbon matrix during (dis)-charging Al/N,S-C battery, we conducted high-resolution XPS analysis on the N,S-C900 cathode before testing (for both S and N) and after fully (dis)-charging (for N in particular). The corresponding XPS spectrum of the S 2p core level of N,S-C900 (before test) is depicted in **Figure S8**, Supporting Information showing the domination of the C-S and C=S components over the C-SO<sub>3</sub><sup>-</sup> specie. On the other hand, the XPS spectra of the N1s core level, shown in **Figure 2c**, reveal the presence of the three characteristic N configurations, i.e., pyridinic N (398.3 eV, before test), pyrrolic N (399.5 eV, before test), and graphitic N (401.2 eV, before test).<sup>[40]</sup> Upon charging up to 2.25 V, the intensity decrease of the pyridinic N 1s signal ( $I_{\text{pd}}$ ) was accompanied by a noticeable increase in the intensity of the graphitic N 1s signal ( $I_{\text{g}}$ ). With its two single electrons on two  $p$ -orbitals, the graphitic N is expected to actively absorb the  $[\text{AlCl}_4]^-$  species, forming new electron pairs and further increasing surface-induced capacity. Compared to the in-plane  $\text{sp}^2$  orbital of pyridinic N, the increasing out-of-plane  $p$ -orbital of graphitic N has contributed extra to the  $d$ -spacing expansion of carbon layers. It is worth noting that the change in the  $I_{\text{g}}/I_{\text{pd}}$  ratio of N,S-C900 was irreversible even upon discharging, indicating a one-way transformation of the N configuration during (dis)-charging cycles.

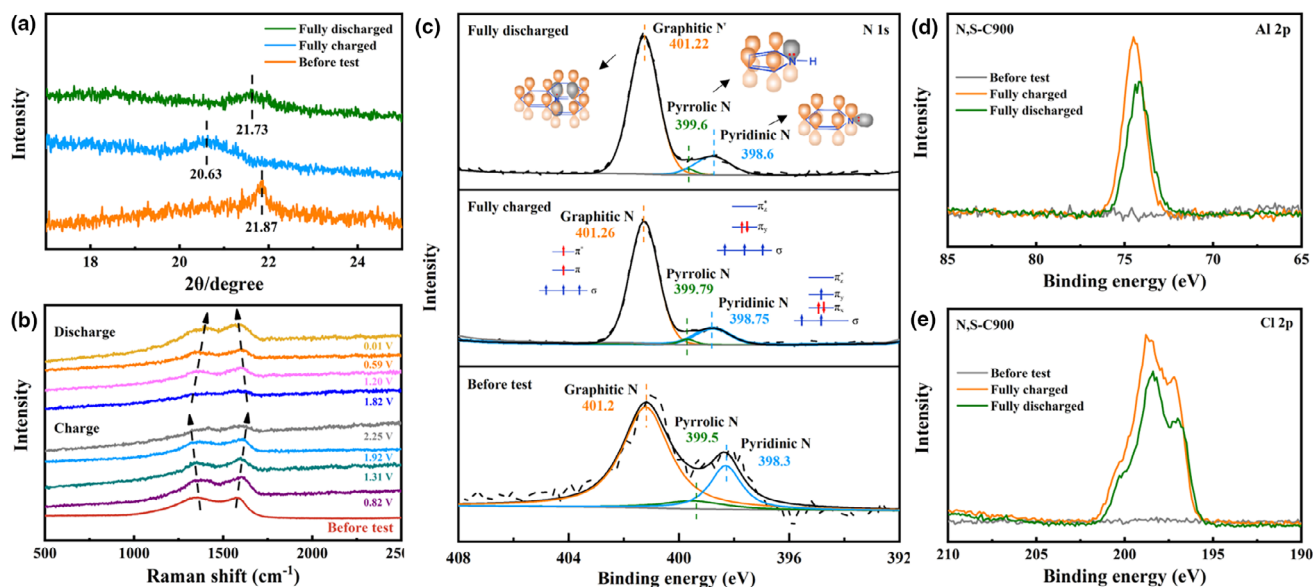


**Figure 2.** a) Ex situ XRD patterns of N,S-C900 cathode before test and after fully (dis)-charged. b) Raman spectra of N,S-C900 measured before test and during (dis)-charging process. c) N 1s core level XPS spectra of N,S-C900 before test and after fully (dis)-charged. d) Al 2p, and e) Cl 2p core level XPS spectra of N,S-C900 before test and after fully (dis)-charged.

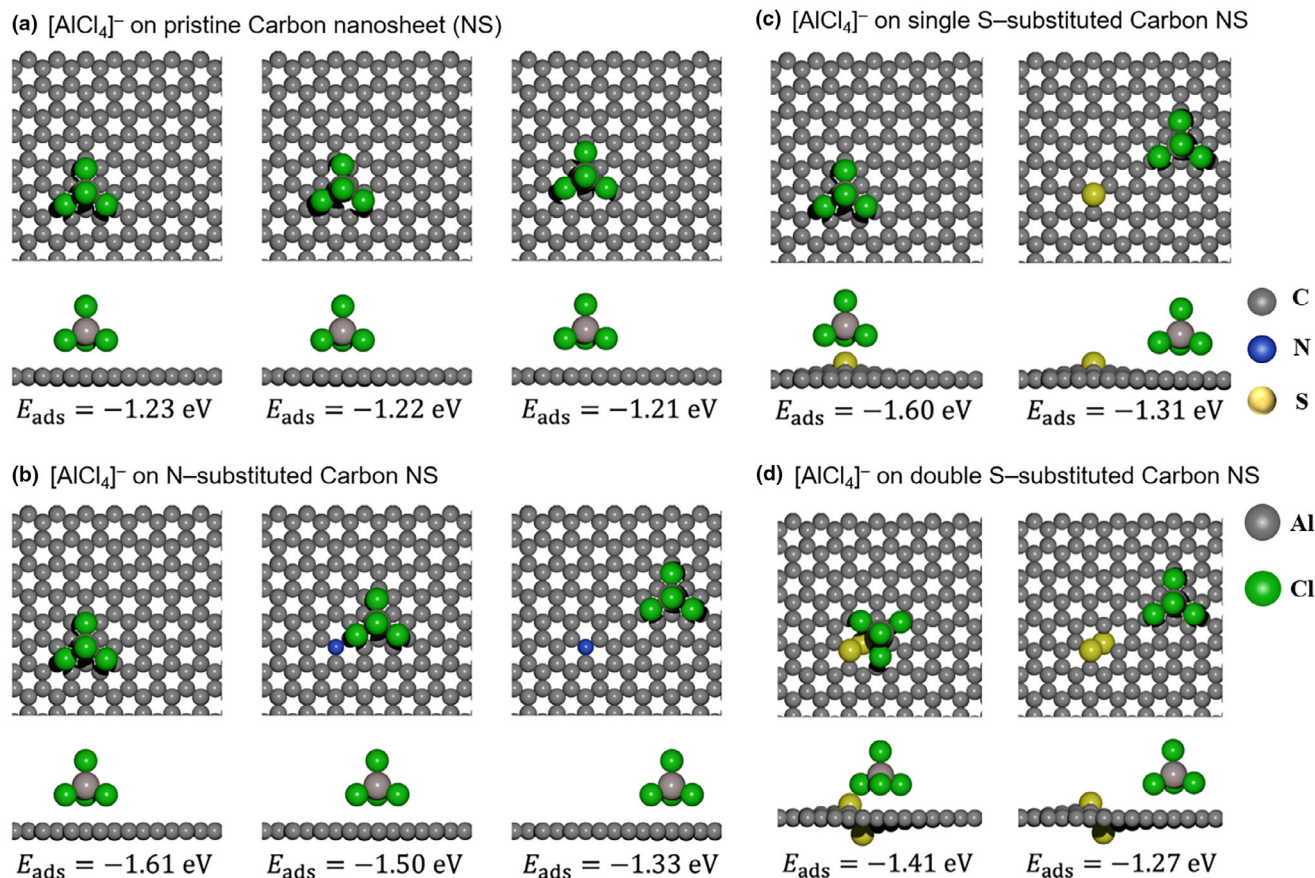


**Figure 3.** Calculated adsorption of  $[\text{AlCl}_4]^-$  at a) pure carbon, and b) N-substituted carbon nanosheet, c, d) two different S-substituted carbon nanosheets, demonstrating top and side views together with corresponding adsorption energies. The N atom is depicted as blue, the sulfur as yellow and the carbon as small grey, while the Al is the larger grey atom surrounded by green Cl atoms.

To model the effect of graphitic nitrogen on the adsorption of  $[\text{AlCl}_4]^-$  species, we compared the adsorption of  $[\text{AlCl}_4]^-$  on ideal carbon nanosheet with and without N-substitutions, by performing periodic density functional theory (DFT) calculations. **Figure 3a,b** illustrate the calculated adsorption energy of  $[\text{AlCl}_4]^-$  at pure carbon and N-substituted carbon nanosheet, indicating that the graphitic nitrogen enhances the adsorption strength, with the lowest energy found when  $[\text{AlCl}_4]^-$  is adsorbed above the N-substitution. The adsorption energies are compared for different adsorption configurations, showing a slight preference for the top site. By moving the  $[\text{AlCl}_4]^-$  away from the N-substitution the adsorption energy approaches that of the pure carbon nanosheet. Usually, other than graphitic N, pyridinic and pyrrolic N have been considered as the major contributors to the enhanced adsorption of cations ( $\text{Na}^+$ ,  $\text{Li}^+$ ) in Sodium-ion or Lithium-ion batteries.<sup>[41,42]</sup> In this case, the major (dis)-intercalating species are negative  $[\text{AlCl}_4]^-$  moieties in aluminum batteries. In addition, we performed DFT calculations to demonstrate whether also S influences the adsorption of  $[\text{AlCl}_4]^-$  (Figure 3c,d). For the sulfur substitution, two different models with a single C atom replaced with a single S atom and with two adjacent C atoms replaced by two S atoms were employed, both demonstrating that S promotes the adsorption of  $[\text{AlCl}_4]^-$ . Combined the DFT simulation with the Raman spectra and XPS analysis, we hypothesize that the N and S both play a critical role in the process of

$[\text{AlCl}_4]^-$  adsorption, leading to enhanced electrochemical performance of the doped carbon cathode.

To demonstrate the redox reaction kinetics and charge transfer resistance of the N,S-C cathodes synthesized under different pyrolysis temperatures (800, 900, and 1000 °C), we performed electrochemical impedance spectroscopy (EIS) for all the fabricated cathodes. The EIS spectra of the N,S-C cathodes (**Figure 4a**) can be divided into a semicircle in the high-frequency zone and a linear part in the low-frequency zone, representing resistance ( $R_{ct}$ ) and ion diffusion ability. According to the EIS-based simulation, the N,S-C900 cathode expressed the smallest  $R_{ct}$  value (29  $\Omega$ ) compared with N,S-C800 (41  $\Omega$ ) and N,S-C1000 (38  $\Omega$ ), indicating its enhanced redox reaction kinetics and electronic conductivity among all the cathodes (more details are provided in [Supporting Information](#)). The relationship between the impedance and the phase angle ( $\theta$ ) of the three cathodes are depicted in **Figure 4b**, which indicating that the N,S-C900 displays the smallest Warburg factor ( $\theta_3$ ), corresponding to the largest  $[\text{AlCl}_4]^-$  diffusion coefficient among the electrodes.

To understand the origin of the reduced  $R_{ct}$  attained by N,S-C900, we measured the work function of the three fabricated cathodes using photoelectron emission spectroscopy in air (PESA). In principle, work function ( $\Phi$ ), usually defined as  $E_{vac} - E_F$ , with  $E_{vac}$  and  $E_F$  denoting the energy of vacuum and Fermi levels, respectively,<sup>[43]</sup> is often used to

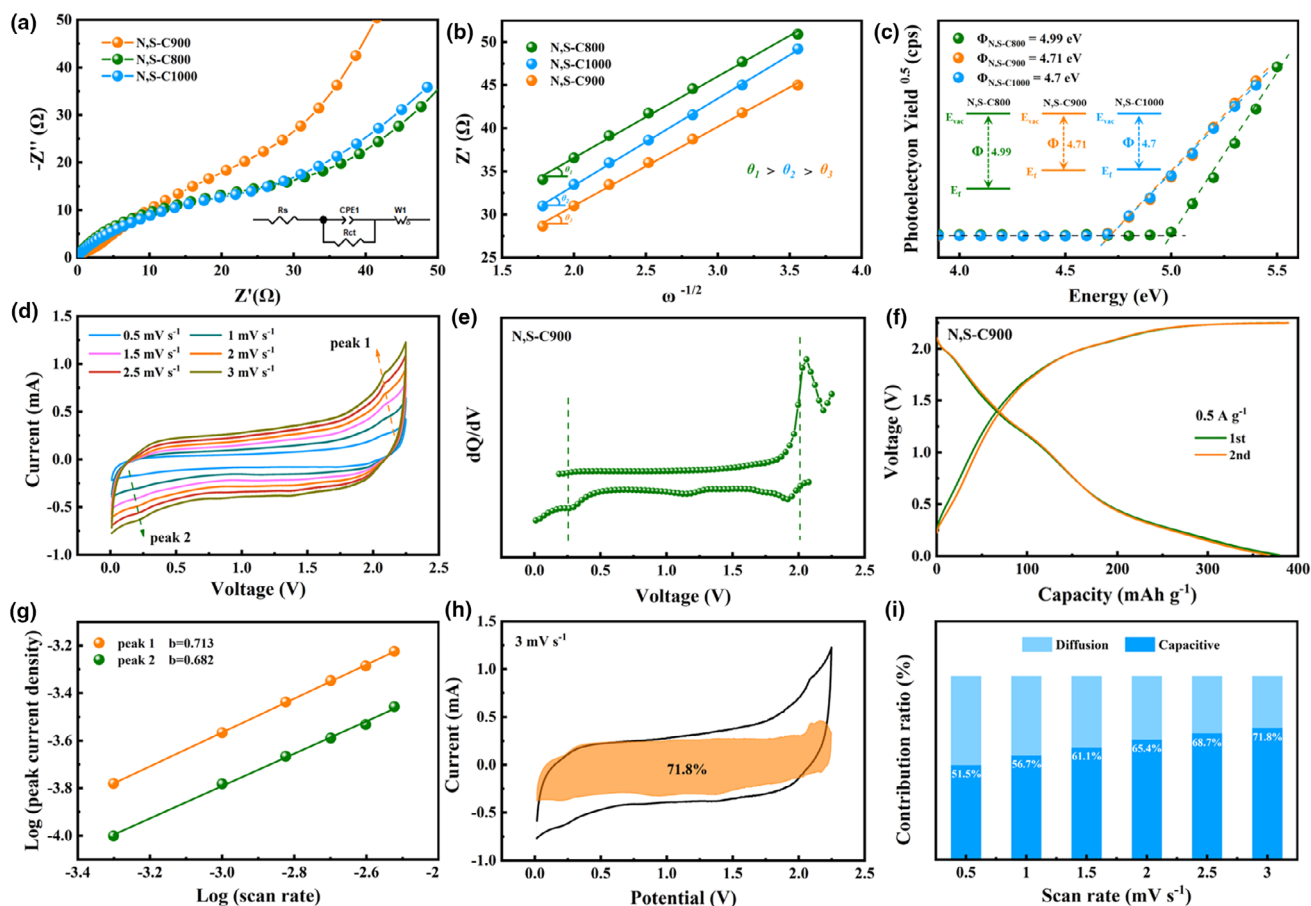


**Figure 4.** a) The EIS spectra. b) Relationship between  $Z_{re}$  and  $\omega^{-1/2}$  in the low-frequency region. c) PESA measurements of the three N,S-C samples and the corresponding extrapolated work functions and PESA-derived schematic energy diagrams for the calcination-induced shifts in the Fermi energy levels in N,S-C samples. d) CV curves of N,S-C900 at different scan rates from 0.5 to  $3 \text{ mV s}^{-1}$ . e)  $dQ/dV$  profile of N,S-C900. f) First and second (dis-)charge profiles of N,S-C900 at a current density of  $0.5 \text{ A g}^{-1}$ . g) Linear slope of  $\log(i)$  versus  $\log(v)$  for N,S-C900. h) Capacitive contribution of N,S-C900 at a sweep rate of  $3 \text{ mV s}^{-1}$ , and i) contribution ratio of the capacitive and diffusion-controlled capacity at various sweep rates.

express the chemical potential of a material (i.e., the ease of charge release).<sup>[44]</sup> Figure 4c presents the photoemission yield spectra of the three N,S-C samples along with extrapolated work function values, i.e., 4.99, 4.71 and 4.7 eV for N,S-C800, N,S-C900 and N,S-C1000, respectively, while a schematic representation of the calcination-induced shift in the Fermi energy level of all the N,S-C samples is depicted in the inset figure. Although both N,S-C900 and N,S-C1000 have expressed nearly the same shift in their work functions (i.e.,  $\sim 300 \text{ meV}$ ), justifying their improved performance compared to N,S-C800, the N,S-C900 cathode has demonstrated a much enhanced performance, thanks to its high surface S content (Table S1, Supporting Information). In principle, when having more oxygen vacancies, the p-orbital single electrons of graphitic N populate more energy states near the Fermi level, decreasing the work function and further promoting the reaction with the  $[\text{AlCl}_4]^-$  species at the N,S-C cathode/electrolyte interface. The cyclic voltammetry (CV) curves of Al/N,S-C900 battery measured with scan rates from 0.5 to  $3 \text{ mV s}^{-1}$  presents a feeble couple of broad redox peaks in Figure 4d, indicating the partial (de-)intercalation mechanism of N,S-C cathodes. Figure 4e displays the  $dQ/dV$  profile of the N,S-C900 cathode, showing the anodic/cathodic

peaks in the range of 0.20–0.25 V and 2.05–2.10 V, indicating a reversible  $[\text{AlCl}_4]^-$  (de-)intercalation within the N,S-C900 interlayers. The first two charge/discharge profiles of N,S-C900 shown in Figure 4f present two inconspicuous voltage plateaus, indicating that the charge-storage mechanism of N,S-C900 cathode is based on surface adsorption/desorption and deintercalation/intercalation of  $[\text{AlCl}_4]^-$  anions, which is consistent with the results of CV curves and  $dQ/dV$  profile. Based on the obtained CV curves,  $dQ/dV$  and (dis-)charge profiles, we propose a mixed storage mechanism of  $[\text{AlCl}_4]^-$  in the N,S-C cathodes comprised of both battery-type intercalation and supercapacitor-type surface absorption. The qualitative analysis of the two separated storage processes can be derived utilizing the equation  $i = av^b$ <sup>[45]</sup> where  $i$  represents the redox peak current under a scan current of rate  $v$ , with  $a$  and  $b$  as constants. The value of the  $b$  constant, equaling 0.5 and 1, indicates independent intercalating behavior and capacitive process, respectively. By plotting the linear slope between  $\log(i)$  and  $\log(v)$ , as shown in Figure 4g, the  $b$ -values of peak 1 and peak 2 for N,S-C900 were respectively derived to be 0.713 and 0.682, revealing a hybrid storage kinetics of  $[\text{AlCl}_4]^-$  within the N,S-C cathodes. The quantitative contribution of capacitive storage can be derived

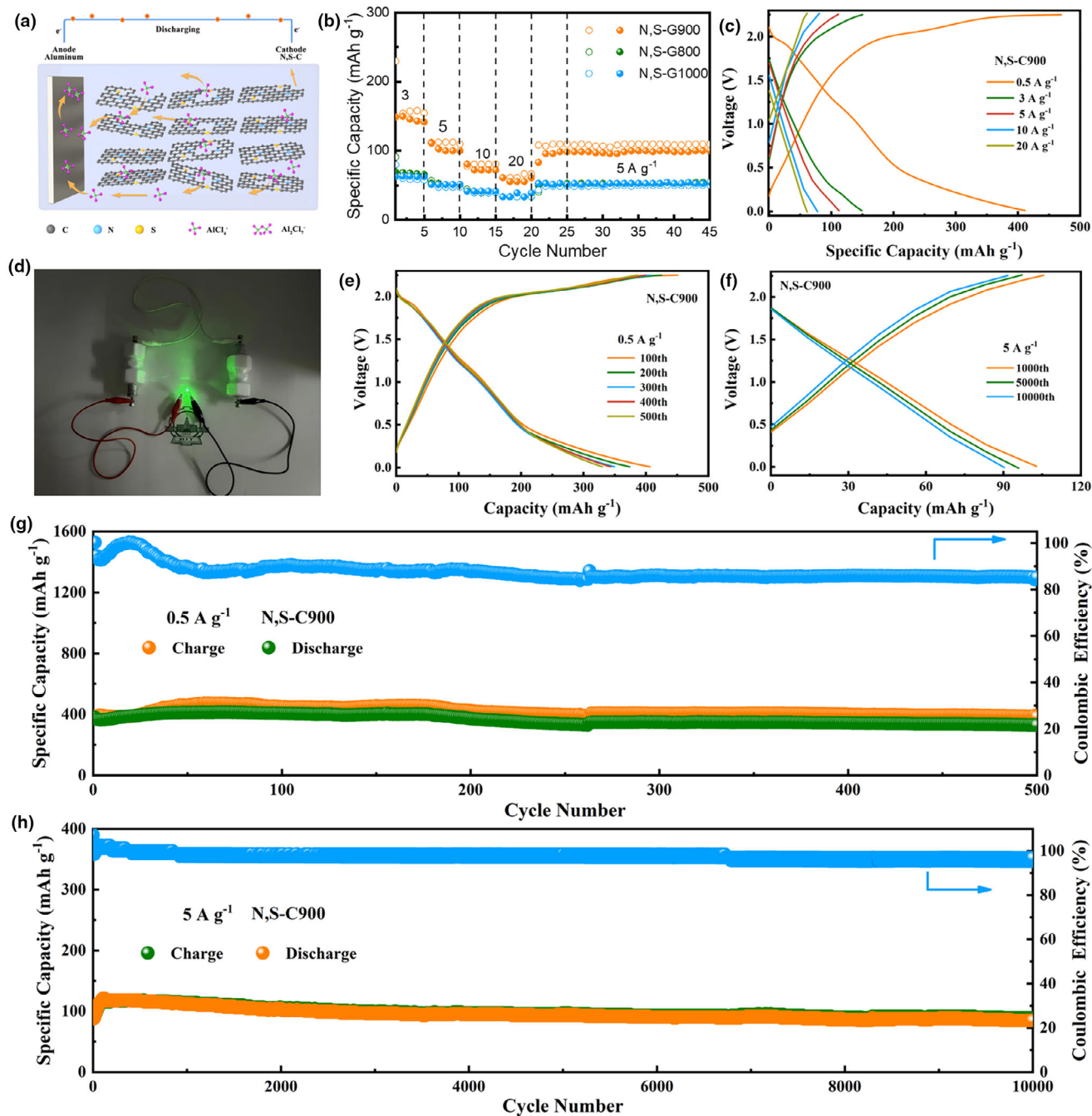


**Figure 5.** a) Schematic illustration of the (dis-)charge process of Al-ion battery embedded with N,S-C cathode. b) Rate performance of the N,S-C cathodes from 3.0 to 20 A g<sup>-1</sup>. c) Typical discharge/charge curves under various current densities of N,S-C900. d) Two serially connected Al/N,S-C batteries for powering a LED lamp. Selected cycles of the N,S-C900 electrode at e) 0.5 A g<sup>-1</sup> and f) 5 A g<sup>-1</sup>. Long-term cycling stability of N,S-C900 at g) 0.5 A g<sup>-1</sup> and h) 5 A g<sup>-1</sup>.

from the equation  $i(V) = k_1\nu + k_2\nu^{1/2}$ , where  $i(V)$  stands for the current at a fixed voltage,  $k_1\nu$  and  $k_2\nu^{1/2}$  represent the intercalating and capacitive contribution, respectively. Figure 4h compares the CV curves for the capacitive contribution (orange region) with the total CV curve at a certain sweep rate of 3 mV s<sup>-1</sup> with the N,S-C900 cathode, and 71.8% capacitive contribution is quantified. Analogously, as shown in Figure 4i, the capacitive contributions at various scan rates are also

calculated and summarized. Similarly, the capacitive contribution ratios for the whole charge storage are 51.5, 56.7, 61.1, 65.4, and 68.7% at sweep rates of 0.5, 1, 1.5, 2, and 2.5 mV s<sup>-1</sup>, respectively. The extra capacity induced by surface absorption is believed to enhance the storage kinetics and high-rate performance of Al/N,S-C batteries.

Figure 5a schematically illustrates the components and the aluminum storage mechanism of the fabricated aluminum batteries. To

demonstrate the practical application potential of the Al/N,S-C battery, two as-assembled batteries were connected in series to light up a light emitting diode (LED) lamp (Figure 5d) by reaching a high voltage of 3.72 V (Figure S9, Supporting Information). Subsequently, we performed the aluminum storage performance of N,S-C electrodes. The rate performances of the assembled Al/N,S-C cells were examined by running the galvanostatic (dis)-charge cycles 50 times at current densities ranging from 0.5 to 20 A g<sup>-1</sup> in the voltage range of 2.25–0.01 V (Figure 5b). As shown in Figure 5c, the discharge/charge curves of the N,S-C900 cathode at different current densities can sustain high capacities, illustrating excellent reversibility and high retention rate of the N,S-C900 cathode. The N,S-C900 cathode exhibited reversible capacities of 410.8, 149.1, 111.0, 80.5, and 61.1 mAh g<sup>-1</sup> at current densities of 0.5, 3, 5, 10 and 20 A g<sup>-1</sup>, respectively, outperforming the rate capacities of N,S-C800 and N,S-C1000 (Figure 5e; Figure S10, Supporting Information). The voltage profiles of the Al/N,S-C900 cell up to 500 cycles at a current density of 0.5 A g<sup>-1</sup> demonstrate a slow capacity decay, confirming the high stability of the developed cathode material. Figure 5g shows the cycling performance and capacity retention of the N,S-C900 cathode carried out at a current density of 0.5 A g<sup>-1</sup> for 500 cycles. The discharge capacity of N,S-C900 experienced a slight decrease from the initial 379.7 mAh g<sup>-1</sup> to 329.6 mAh g<sup>-1</sup> at the 500th cycle, whereas the Coulombic efficiency gradually dropped from ~98% to ~85%. The discharge curves of the N,S-C900 cathode at higher charging rates (1 A g<sup>-1</sup>) have also exhibited two discharging regions induced by de-intercalation and de-absorption of [AlCl<sub>4</sub>]<sup>-</sup> (Figure S11a, Supporting Information). Generally, the N,S-C900 cathode has exhibited remarkable reversible capacities around 330 mAh g<sup>-1</sup> at a current density of 0.5 A g<sup>-1</sup> over 500 cycles, superior to the previously reported carbon-based and transition metal-related cathode materials for AIBs (Table S3). The cycling profile of N,S-C900 at a current density of 1 A g<sup>-1</sup> presented a discharge capacity of 213 mAh g<sup>-1</sup> with a Coulombic efficiency of 87% after 600 cycles (Figure S11b, Supporting Information). Notably, N,S-C900 delivered excellent long-term cycling performance as well at higher rates, sustaining a capacity of ~90 mAh g<sup>-1</sup> after 10 000 cycles with a 100% coulombic efficiency at a high rate of 5 A g<sup>-1</sup> (Figure 5h) and a low capacity decay rate of 0.03% in per cycle (Figure 5f). However, N,S-C800 and N,S-C1000 underwent rapid capacity decay or undesirable capacity in Figure S12, Supporting Information. The relatively low rate capacity of N,S-C800 can be ascribed to the high defect concentration caused by its low crystallinity and high R<sub>ct</sub> value (41 Ω), resulting in a high diffusion barrier and sluggish intercalating kinetics of [AlCl<sub>4</sub>]<sup>-</sup> between cathode interlayers. Even with high crystallinity and a work function matching that of N,S-C900, the low N doping concentration (3.78%) made N,S-C1000 unable to provide enough active sites for the absorption of [AlCl<sub>4</sub>]<sup>-</sup> moieties, consequently leading to inadequate capacitive contribution to energy storage. Specifically, the low S content ratio of N,S-C800 (0.29%) and N,S-C1000 (0.38%) are partially responsible of their inferior electrochemical performances. In addition, to explore whether the Al/N,S-C battery can work properly under extreme conditions, we evaluated its performance at high temperatures. The N,S-C900 showing a discharge capacity of ~76 mAh g<sup>-1</sup> with a coulombic efficiency of 95% after 1800 cycles at 5 A g<sup>-1</sup> in a 60 °C oven (Figure S11c,d, Supporting Information), and presenting a discharge capacity of ~60 mAh g<sup>-1</sup> with a coulombic efficiency of 98% after 1000 cycles at 5 A g<sup>-1</sup> in a 80 °C oven (Figure S11e,f, Supporting Information), further indicating the practical application prospects. In addition, we further characterized the morphology and Raman

spectrum of the N,S-C900 cathode after 100 cycles. It can be clearly observed that N,S-C still maintained the original nanosheet morphology without the rupture of the carbon layer and the D band and G band of N,S-C900 are also clearly visible, which are indicative of its excellent durability and structural stability (Figure S13, Supporting Information). Generally, the performance of N,S-C900 cathode is superior to most of the previously reported carbon-based and transition metal-related cathode materials for AIBs (Table S3, Supporting Information).

Based on the characterizations of the fabricated cathode materials and their corresponding electrochemical properties, we were able to develop a clear understanding of the underlying mechanisms of the [AlCl<sub>4</sub>]<sup>-</sup> storage in the developed Al/N,S-C batteries, as follows: 1) Doping the C<sub>3</sub>N<sub>4</sub>-derived carbon frameworks with N and S heteroatoms have led to the expansion of the interlayer d-spacing, accelerating the diffusion-controlled intercalation kinetics of [AlCl<sub>4</sub>]<sup>-</sup>. 2) The multiple N configurations have provided plenty of active sites for the [AlCl<sub>4</sub>]<sup>-</sup> adsorption, generating additional surface-induced capacity: Upon charging, part of the pyridinic N, with a lone pair occupying an sp<sup>2</sup> orbital, was irreversibly converted to graphitic N with two single electrons on two p-orbitals, inevitably increasing the probability of forming electron pairs of N/[AlCl<sub>4</sub>]<sup>-</sup>, which can be evidenced by the gradual disappearance of the D-band in Raman spectra of N,S-C900 during the charging process. The increased bonding between graphitic N and [AlCl<sub>4</sub>]<sup>-</sup> has significantly enhanced the surface absorption-derived capacity. 3) The doped S atoms, exhibiting less electronegativity than O terminations, have assisted with the fast (de)-intercalation of [AlCl<sub>4</sub>]<sup>-</sup>. Owing to the above mentioned unique features, the N,S-C900 cathode has offered an advanced [AlCl<sub>4</sub>]<sup>-</sup> storage performance in AIBs with excellent stability.

### 3. Conclusions

In conclusion, N,S-C900 was successfully demonstrated as a high-capacity cathode material for AIBs with outstanding structural stability, delivering a reversible capacity of 330 mAh g<sup>-1</sup> at a current density of 0.5 A g<sup>-1</sup> over 500 cycles, combining the contribution of both intercalation and surface absorption of [AlCl<sub>4</sub>]<sup>-</sup>. When performed at a high rate of 5 A g<sup>-1</sup>, the Al/N,S-C900 battery exhibited ultrahigh reversible stability over 10 000 cycles with a capacity retention of 97%. The excellent performance of the N,S-C900 cathode was mainly attributed to the tunable configurations of the doped N heteroatoms and expanded interlayer spacing. We believe that the reduced work function and electron pairing between the p-orbital single electrons of graphitic N and the extra electrons of the negative [AlCl<sub>4</sub>]<sup>-</sup> moieties has enhanced the interaction between the N,S-C900 cathode and the present ionic groups at the cathode/electrolyte interface, significantly contributing to the surface absorption-induced capacity. The successful realization of highly reversible Al/N,S-C900 battery encompassing dual reinforcement of intercalation and absorption provides a general methodology for designing cathodes with high capacities for efficient AIBs operating at different temperatures. However, further research is still needed to extend the attained capacity ceiling at much lower costs.

### 4. Experimental Section

**Experimental material:** Five gram of melamine was added to a combustion boat and then transferred to a tube furnace for calcination. With a heating rate of 4

$^{\circ}\text{C min}^{-1}$ , melamine was thermally treated at  $500^{\circ}\text{C}$  for 3 h to obtain bulk  $\text{g-C}_3\text{N}_4$ , which was further cooled down to room temperature and smashed to a powder-like final product. After mixing 2 g of  $\text{g-C}_3\text{N}_4$  with 0.375 g of anhydrous glucose, 0.375 g of dithiooxamide, and 2 ml of absolute ethanol, the mixture was ball milled for 6 h to obtain homogeneous reactant. After drying in a vacuum oven at  $60^{\circ}\text{C}$  for 5 h to remove the ethanol, the reactant was heated to  $700^{\circ}\text{C}$  for 3 h at a heating rate of  $3^{\circ}\text{C min}^{-1}$  under argon atmosphere, followed by heating to  $800\text{--}1000^{\circ}\text{C}$  for 3 h at a heating rate of  $4^{\circ}\text{C min}^{-1}$ . Dithiooxamide started to decompose at high temperatures (above 700 degrees), yielding hydrogen sulfide ( $\text{H}_2\text{S}$ ), carbon disulfide ( $\text{CS}_2$ ), and nitrogen gas ( $\text{N}_2$ ), while nitrogen (N) and sulfur (S) grew on the carbon template simultaneously. Different heating temperatures result in variations in the N and S contents on the carbon substrate, obtaining different N,S-doped carbon cathodes, i.e., N,S-C800, N,S-C900, and N,S-C1000.

**Materials characterization:** The morphologies of N,S-C were investigated by SEM (Zeiss Merlin) and TEM. X-ray diffraction (XRD, Bruker D8 Advance) and X-ray photoelectron spectroscopy (XPS, Amicus) were utilized to study the evolution of microstructure and surface chemistry of materials. Raman spectroscopy was carried out with a 532 nm laser excitation on a Raman Microscope (Horiba LabRAM HR). HRTEM was performed to get an insight into the atomic range of carbon frameworks. Photoemission spectroscopy in air (PESA) system (model AC-2 from RKI Instruments Inc.) was used to measure the work function. During the PESA measurements, the N,S-C samples were irradiated with a tunable-energy UV source in the range of 3.6–6.2 eV at an intensity of 100 nW.

**Assembly of Al<sup>3+</sup> ion batteries and electrochemical measurements:** The N,S-C based cathodes were fabricated by proportionally mixing N,S-C with carbon black powders and polyvinylidene fluoride (PVDF) at a mass ratio of 7:2:1 in NMP solvent. The final cathodes were prepared by casting the mixture on a molybdenum foil collector and drying at  $110^{\circ}\text{C}$  under vacuum for 12 h. With effective loading of  $\sim 1.0\text{ mg cm}^{-2}$ , N,S-C cathodes were assembled with aluminum foil anode, [EMIm]Cl/AlCl<sub>3</sub> electrolyte, and Whatman GF/C separator in the glovebox to fabricate Swagelok Al/N,S-C batteries. The EIS test with the frequency range from 1 to 100 MHz was performed by Gamry Interface 5000 electrochemical workstation. The electrochemical performance of all the Al/N,S-C batteries was examined by performing CV measurements using the same workstation in a voltage window from 0.01 to 2.25 V at a scan rate ranging from 0.5 to  $3\text{ mV s}^{-1}$ .

**Computational details:** Periodic density functional theory calculations were performed with the VASP code<sup>[46]</sup> using the projector-augmented wave method to describe core electrons<sup>[47]</sup> and with planewaves expanded to a kinetic energy cutoff of 450 eV. The van der Waals density functional<sup>[48,49]</sup> described exchange-coordination effects, with the version of Hamada denoted as rev-vdWDF2. The layered carbon systems were represented using the computed lattice constant of carbon of 2.466 Å. For all calculations, a  $p(10 \times 10)$  supercell of carbon was used together with a  $4 \times 4 \times k$ -point sampling. To minimize the interaction between periodic images the carbon layers were separated by a vacuum region of 30 Å. For the nitrogen-substituted system, one of the carbon atoms was replaced by nitrogen while keeping the size of the unit cell fixed. All structures were structurally optimized until the residual forces on all atoms were smaller than 0.01 eV/Å. Adsorption energies for  $[\text{AlCl}_4]^-$  were calculated as the energy difference of  $[\text{AlCl}_4]^-$  adsorbed on the surface and  $[\text{AlCl}_4]^-$  placed in the middle of the vacuum region. It should be noted that calculations were performed on neutral systems. The Bader charge of  $[\text{AlCl}_4]^-$  adsorbed on carbon was found to be  $-1\text{e}$ , while in the desorbed state it had a Bader charge of  $-0.7\text{e}$ , i.e., only a marginal part of the adsorption energy is due to charge transfer between AlCl<sub>4</sub> and carbon, and the calculated values give a good description of  $[\text{AlCl}_4]^-$  adsorption.

## Acknowledgements

J.L., J.K.E.-D. and G.S. contributed equally to this work. The authors appreciate the financial support from the National Natural Science Foundation of China (Grand No. 52203092). J.R. acknowledges funding from an SSF Synergy Program (EM16-0004). The computations were enabled by resources provided by the National Academic Infrastructure for Supercomputing in Sweden (NAISS) funded by the Swedish Research Council through grant agreement no. 2022-06725.

## Conflict of Interest

The authors declare no conflict of interest.

## Supporting Information

Supporting Information is available from the Wiley Online Library or from the author.

## Keywords

2D carbon, adsorption energy, heteroatoms-doping, high capacity, long cycling life

Received: December 23, 2023

Revised: January 11, 2024

Published online: January 30, 2024

- [1] F. Wu, H. Yang, Y. Bai, C. Wu, *Adv. Mater.* **2019**, *31*, 1806510.
- [2] D. Yu, K. Li, G. Ma, F. Ru, X. Zhang, W. Luo, P. Hu, D. Chen, H. Wang, *ChemSusChem* **2023**, *16*, e202201595.
- [3] N. P. Stadie, S. Wang, K. V. Kravchik, M. V. Kovalenko, *ACS Nano* **2017**, *11*, 1911.
- [4] S. Wang, K. V. Kravchik, F. Krumeich, M. V. Kovalenko, *ACS Appl. Mater. Interfaces* **2017**, *9*, 28478.
- [5] M. Walter, K. V. Kravchik, C. Böfer, R. Widmer, M. V. Kovalenko, *Adv. Mater.* **2018**, *30*, 1705644.
- [6] K. V. Kravchik, M. V. Kovalenko, *Adv. Energy Mater.* **2019**, *9*, 1901749.
- [7] B. Wang, Y. Huang, Y. Wang, H. Wang, *Adv. Funct. Mater.* **2023**, *33*, 2212287.
- [8] F. Ambroz, T. J. Macdonald, T. Nann, *Adv. Energy Mater.* **2017**, *7*, 1602093.
- [9] S. K. Das, S. Mahapatra, H. Lahan, *J. Mater. Chem. A* **2017**, *5*, 6347.
- [10] N. Jayaprakash, S. K. Das, L. A. Archer, *Chem. Commun.* **2011**, *47*, 12610.
- [11] T. Koketsu, J. Ma, B. J. Morgan, M. Body, C. Legein, W. Dachraoui, M. Giannini, A. Demortière, M. Salanne, F. Dardoize, H. Groult, O. J. Borkiewicz, K. W. Chapman, P. Strasser, D. Dambournet, *Nat. Mater.* **2017**, *16*, 1142.
- [12] Y. Hu, D. Ye, B. Luo, H. Hu, X. Zhu, S. Wang, L. Li, S. Peng, L. Wang, *Adv. Mater.* **2018**, *30*, 1703824.
- [13] J.-M. Cao, I. V. Zatorovsky, Z.-Y. Gu, J.-L. Yang, X.-X. Zhao, J.-Z. Guo, H. Xu, X.-L. Wu, *Prog. Mater. Sci.* **2023**, *135*, 101105.
- [14] M.-C. Lin, M. Gong, B. Lu, Y. Wu, D.-Y. Wang, M. Guan, M. Angell, C. Chen, J. Yang, B. Hwang, H. Dai, *Nature* **2015**, *520*, 325.
- [15] C. Li, S. Dong, R. Tang, X. Ge, Z. Zhang, C. Wang, Y. Lu, L. Yin, *Environ. Sci.* **2018**, *11*, 3201.
- [16] A. VahidMohammadi, A. Hadjikhani, S. Shahbazmohamadi, M. Beidaghi, *ACS Nano* **2017**, *11*, 11135.
- [17] J. Li, F. Zeng, J. K. El-Demellawi, Q. Lin, S. Xi, J. Wu, J. Tang, X. Zhang, X. Liu, S. Tu, *ACS Appl. Mater. Interfaces* **2022**, *14*, 45254.
- [18] S. Guo, Z. Deng, M. Li, B. Jiang, C. Tian, Q. Pan, H. Fu, *Angew. Chem. Int. Ed. Engl.* **2016**, *55*, 1830.
- [19] X. Wang, G. Sun, P. Routh, D. H. Kim, W. Huang, P. Chen, *Chem. Soc. Rev.* **2014**, *43*, 7067.
- [20] Y. Liu, Y. Qiao, G. Wei, S. Li, Z. Lu, X. Wang, X. Lou, *Energy Storage Mater.* **2018**, *11*, 274.
- [21] J. Xu, M. Wang, N. P. Wickramaratne, M. Jaroniec, S. Dou, L. Dai, *Adv. Mater.* **2015**, *27*, 2042.
- [22] H.-G. Wang, Z. Wu, F.-L. Meng, D.-L. Ma, X.-L. Huang, L.-M. Wang, X.-B. Zhang, *ChemSusChem* **2013**, *6*, 56.

- [23] X. Wang, X. Cao, L. Bourgeois, H. Guan, S. Chen, Y. Zhong, D.-M. Tang, H. Li, T. Zhai, L. Li, Y. Bando, D. Golberg, *Adv. Funct. Mater.* **2012**, *22*, 2682.
- [24] X. Liu, J. Zhang, S. Guo, N. Pinnad, *J. Mater. Chem. A* **2016**, *4*, 1423.
- [25] J. Liu, Y. Zhang, L. Zhang, F. Xie, A. Vasileff, S.-Z. Qiao, *Adv. Mater.* **2019**, *31*, 1901261.
- [26] Z. Liu, Y. Zhu, J. K. El-Demellawi, D. B. Velusamy, A. M. El-Zohry, O. M. Bakr, O. F. Mohammed, H. N. Alshareef, *ACS Energy Lett.* **2019**, *4*, 2315.
- [27] Y. Cao, L. Xiao, M. L. Sushko, W. Wang, B. Schwenzer, J. Xiao, Z. Nie, L. V. Saraf, Z. Yang, J. Liu, *Nano Lett.* **2012**, *12*, 3783.
- [28] G. Wang, M. Yu, X. Feng, *Chem. Soc. Rev.* **2021**, *50*, 23882443.
- [29] R. D. Mckerracher, A. Holland, A. Cruden, R. G. A. Wills, *Carbon* **2019**, *144*, 333e341.
- [30] F. Tuinstra, J. L. Koenig, *J. Chem. Phys.* **1970**, *53*, 1126.
- [31] L. G. Cançado, A. Jorio, E. H. M. Ferreira, F. Stavale, C. A. Achete, R. B. Capaz, M. V. O. Moutinho, A. Lombardo, T. S. Kulmala, A. C. Ferrari, *Nano Lett.* **2011**, *11*, 3190.
- [32] A. C. Ferrari, D. M. Basko, *Nat. Nanotechnol.* **2013**, *8*, 235.
- [33] S. Wang, L. Xia, L. Yu, L. Zhang, H. Wang, X. W. Lou, *Adv. Energy Mater.* **2016**, *6*, 1502217.
- [34] Z.-Q. Liu, H. Cheng, N. Li, T. Y. Ma, Y.-Z. Su, *Adv. Mater.* **2016**, *28*, 3777.
- [35] W.-H. Li, Q.-L. Ning, X.-T. Xi, B.-H. Hou, J.-Z. Guo, Y. Yang, B. Chen, X.-L. Wu, *Adv. Mater.* **2019**, *31*, 1804766.
- [36] B. A. Lindquist, T. H. Dunning, *Theor. Chem. Accounts* **2014**, *133*, 1443.
- [37] M. A. Reddy, M. Helen, A. Groß, M. Fichtner, H. Euchner, *ACS Energy Lett.* **2018**, *3*, 2851.
- [38] D. Y. Wang, C. Y. Wei, M. C. Lin, C. J. Pan, H. L. Chou, H. A. Chen, M. Gong, Y. Wu, C. Yuan, M. Angell, Y. J. Hsieh, Y. H. Chen, C. Y. Wen, C. W. Chen, B. J. Hwang, C. C. Chen, H. Dai, *Nat. Commun.* **2017**, *8*, 14283.
- [39] C. Thomsen, S. Reich, *Phys. Rev. Lett.* **2000**, *85*, 5214.
- [40] D. Wei, Y. Liu, Y. Wang, H. Zhang, L. Huang, G. Yu, *Nano Lett.* **2009**, *9*, 1752.
- [41] J. Zhang, Q. Zhang, X. Qu, G. Xu, B. Fan, Z. Yan, B. Feng, F. Gui, L. Yang, *Appl. Surf. Sci.* **2022**, *574*, 151559.
- [42] C. Ma, X. Shao, D. Cao, *J. Mater. Chem.* **2012**, *22*, 8911.
- [43] J. K. El-Demellawi, A. E. Mansour, A. M. El-Zohry, M. N. Hedhili, J. Yin, A.-H. M. Emwas, P. Maity, X. Xu, O. M. Bakr, O. F. Mohammed, H. N. Alshareef, *ACS Mat. Lett.* **2022**, *4*, 2480.
- [44] Y. Gao, Z. Wang, L. Chen, *J. Mater. Chem. A* **2015**, *3*, 23420.
- [45] H. Lindström, S. Södergren, A. Solbrand, H. Rensmo, J. Hjelm, A. Hagfeldt, S.-E. Lindquist, *J. Phys. Chem. B* **1997**, *101*, 7717.
- [46] G. Kresse, J. Furthmüller, *Phys. Rev. B* **1994**, *54*, 11169.
- [47] P. E. Blöchl, *Phys. Rev. B* **1994**, *50*, 17953.
- [48] M. Dion, H. Rydberg, E. Schröder, D. C. Langreth, B. I. Lundqvist, *Phys. Rev. Lett.* **2004**, *92*, 246401.
- [49] I. Hamada, *Phys. Rev. B* **2014**, *89*, 121103(R).